Angular momentum projection in the deformed relativistic Hartree-Bogoliubov theory in continuum

Xiang-Xiang Sun (孙向向)[1,2] and Shan-Gui Zhou (周善贵)[2,3,4,5,*]

[1]*School of Nuclear Science and Technology, University of Chinese Academy of Sciences, Beijing 100049, China*
[2]*CAS Key Laboratory of Theoretical Physics, Institute of Theoretical Physics, Chinese Academy of Sciences, Beijing 100190, China*
[3]*School of Physical Sciences, University of Chinese Academy of Sciences, Beijing 100049, China*
[4]*Center of Theoretical Nuclear Physics, National Laboratory of Heavy Ion Accelerator, Lanzhou, 730000, China*
[5]*Synergetic Innovation Center for Quantum Effects and Application, Hunan Normal University, Changsha 410081, China*

(Received 23 July 2021; revised 25 October 2021; accepted 7 December 2021; published 22 December 2021)

The angular momentum projection (AMP) method is implemented in the deformed relativistic Hartree-Bogoliubov theory in continuum (DRHBc) with the point-coupling density functional. The wave functions of angular momentum projected states are expanded in terms of the Dirac Woods-Saxon (WS) basis, providing a proper description of the asymptotic behavior of the wave functions. The contribution of continuum induced by the pairing is considered by treating the pairing correlation with the Bogoliubov transformation. We present the formulas and numerical checks for the DRHBc+AMP approach in detail and use it to study low-lying excited states of axially deformed nuclei. Our calculations show that neutron-rich magnesium isotopes ^{36,38,40}Mg are all well-deformed nuclei. The low-lying spectra of these three nuclei are obtained. The ground-state rotational bands of ^{36,38,40}Mg are reproduced reasonably well by using this new DRHBc+AMP approach with the density functional PC-F1.

DOI: 10.1103/PhysRevC.104.064319

I. INTRODUCTION

With the development of the radioactive-ion-beam facilities, many exotic nuclear phenomena which differ from the properties of nuclei close to the β-stability line have been observed, including proton or neutron halos [1,2], changes of the nuclear magic numbers [3–6], the island of inversion [7], neutron skin [8], clustering effects [9,10], new radioactivities [11], nuclear bubble structure [12,13], shape coexistence [14–16], etc. The study of these exotic structures is at the frontier of nuclear physics nowadays [10,15,17–25]. The description of the structure of exotic nuclei has been achieved by using many approaches, e.g., the shell model (SM) approach [25,26], nuclear density functional theory (NDFT) [17,19,22,27], antisymmetrized molecular dynamics [28], and few-body models [29]. One of the advantages of the NDFT is that it can describe almost all nuclei in the nuclear chart with global density functionals, especially for heavy and superheavy nuclei.

The basic implementation of NDFT is achieved by using self-consistent mean-field (SCMF) methods, in which the total energy of the system is constructed as a functional of one-body local nucleon density [21]. The bulk properties of finite nuclei, including binding energy, radius, deformation, etc., have been successfully described by using SCMF methods [17,19,22,27,30,31]. In general, the wave function obtained from mean-field (MF) calculations in the intrinsic frame is approximated by a generalized Slater determinant of the Hartree-Fock-Bogoliubov (HFB) type and allowed to break symmetries of the Hamiltonian, such as particle number conservation and rotational and translational invariances [17,22,30,32–34]. As a consequence, the MF wave function cannot be used to study correlations corresponding to the spontaneous symmetry breaking, quantum fluctuation of collective degrees of freedom, spectroscopic observable in the laboratory frame, and selection rules of the transitions. These deficiencies can be complemented via beyond-mean-field (BMF) calculations based on SCMF methods [32,35]. The violation of the SO(3) symmetry in the intrinsic frame for deformed nuclei and U(1) symmetry in the gauge space for superfluid nuclei can be restored by using the angular momentum projection (AMP) and particle number projection (PNP), respectively [22,32,33]. The quantum fluctuation of collective degrees of freedom is usually treated with the generator coordinate method (GCM) [32]. In principle, these broken symmetries should be restored by using projection before variation (PBV) calculations [32], which are technically very complicated and have been rarely achieved in NDFT, especially for the case of the AMP; see, e.g., Ref. [35] for a recent review. Usually the projection after variation (PAV) approach is adopted to restore the broken symmetries within the framework of NDFT.

The AMP has been successfully implemented in nonrelativistic and relativistic MF models (see Refs. [17,21,30,34,35] and references therein) and has been used to explain or predict many exotic nuclear structures connected with the nuclear collective excitation, for instance, the structure of low-spin and high-spin states [36–38], shape coexistence in Kr and Pb isotopes [39,40], shell evolution in neutron-rich Ti and Cr

*sgzhou@itp.ac.cn

isotopes [41], shape transitions [42,43], low-lying excitation of hypernuclei [44–47], excitation of triaxially deformed nuclei [48–54], nuclear octupole excitation [55–58], and the structure and fission of superheavy nuclei [59–61]. In addition, it is worth mentioning that the BMF calculations have been performed to study the excitation of odd-$N(Z)$ nuclei [62–65].

It should be noted that in the above-mentioned calculations with the AMP, the wave functions of the intrinsic and excited states are almost all expanded in terms of the harmonic oscillator (HO) wave functions [66–68]. The HO wave functions can be obtained analytically and have great advantages for numerical treatments. But it has been shown in Refs. [69–72] that the asymptotic behavior of the wave functions for weakly bound and low-l orbitals cannot be described properly with this basis in the MF ground states, even if the size of the basis space is taken to be very large. Therefore expanding the wave functions of angular momentum projected states in terms of the HO basis is also not suitable to describe the asymptotic behavior of the densities for loosely bound nuclei close to drip lines, including halo nuclei.

Nuclear halos are characterized by the large spatial extension and formed in loosely bound nuclei when the valence nucleons close to the threshold of particle emission occupy low l (s- or p-wave) orbitals with considerable amplitudes [73–79]. Therefore, when studying halo nuclei by employing SCMF approaches, the single-particle wave functions are usually obtained in coordinate (r) space by using the shooting and matching method [77,80], the finite element solution [81], and the Lagrange-mesh method [82]. Alternatively, in configuration space, the wave function can be expanded by a set of proper basis functions, such as the Woods-Saxon (WS) basis [71], the Gaussian basis [83], and the transformed HO basis [69,84]. Pairing correlations play a vital role in the formation of halos and are usually treated by using the Bogoliubov transformation [74,77,80]. For spherical halo nuclei, by solving the Hartree-Fock-Bogoliubov (HFB) or relativistic Hartree-Bogoliubov (RHB) equation with spherical potentials, the ground-state property [75,77,85–87] can be well described. Deformation-driven halos are common for halo nuclei in medium mass region, such as those observed in ^{31}Ne [88,89] and ^{37}Mg [90]. Within the framework of SCMF, the first self-consistent study of deformed halo nuclei has been achieved by using the deformed relativistic Hartree-Bogoliubov theory in continuum (DRHBc) [91], and after that many deformed halo nuclei have been predicted by using MF approaches [83,92–97]. The establishment of rotational bands of deformed halo nuclei is helpful to understand the halo structure and configuration [89]. Therefore in the framework of DFT, it is necessary to apply the BMF method to study deformed halo nuclei [98].

The covariant density functional theory (CDFT) has become a powerful tool to study the properties of stable and exotic nuclei over the whole nuclear chart with universal density functionals [19–22,27,99–101]. For the study of halo nuclei within the framework of the CDFT, the relativistic continuum Hartree-Bogoliubov (RCHB) [75–77,102] and relativistic HFB theories [87,103] have been developed for spherical halos and the DRHBc theory based on the Dirac WS basis for deformed ones [91,94]. When studying halos in deformed nuclei, shape decoupling effects originated from the intrinsic structure of valence levels have been predicted by using the DRHBc theory [91]. Deformed halos with shape decoupling effects in C, Ne, and Mg isotopes have been revealed by using this theory [91,94–97]. Specifically, the DRHBc theory can well explain the halo structures in ^{17,19}B [104,105]. In addition, the construction of the DRHBc nuclear mass table is in progress [106–110].

Within the framework of the CDFT, the implementation of AMP in the relativistic mean field (RMF) models with the HO basis has been realized [21]. In Refs. [111,112], the BMF methods for axially deformed nuclei with spatial reflection symmetry have been developed. Three-dimensional (3D) AMP [47,50,51,113] has been applied to study low-lying excited states of triaxially deformed nuclei. Beyond RMF approaches have been also used to investigate nuclear octupole excitations [55]. Recently, an AMP method based on the multidimensionally constrained (MDC) CDFTs [23,114–116] has been developed [117]. The calculations by using MDC-CDFTs+AMP can describe the properties of both the ground state in the MF level and low-lying excited states in the laboratory frame for systems with various deformations, such as β_{20}, β_{22}, β_{30}, β_{32}, β_{40}, etc., in a microscopic and self-consistent way. It is desirable to develop the AMP based on the DRHBc theory to study the properties of the collective motion for deformed nuclei.

In the DRHBc theory, the MF wave function is expanded in terms of the Dirac WS basis, which can also be used to construct the angular momentum projected states. In this way, a proper description of the asymptotic behavior of the wave functions in excited states is achieved. The angular momentum projection after variation has been developed based on the DRHBc theory, aiming at a microscopic description of low-lying excitation of the deformed nuclei, especially for deformed halo nuclei. As a first application of the DRHBc+AMP approach, the rotational excitation of a deformed halo nucleus was explored and it was found that both the halo structure and shape decoupling effects can appear in rotational excited states [98]. In this work we take ^{36,38,40}Mg as examples and present in detail how to implement the AMP into the DRHBc theory, careful numerical checks, and the study of ground-state rotational bands of these three nuclei.

This paper is organized as follows. The main formulas of the DRHBc+AMP approach are given in Sec. II. We perform numerical checks of this newly developed approach in Sec. III. The applications on ^{36,38,40}Mg are given and discussed in Sec. IV. We summarize this work in Sec. V.

II. THEORETICAL FRAMEWORK

A. The DRHBc theory

The DRHBc theory with both the meson-exchange [91,94,118,119] and point-coupling [106] effective interactions have been developed. The AMP is implemented based on the point-coupling density functionals. Here we introduce the main formulas of the DRHBc theory with the point-coupling density functionals. Under the MF and no-sea approximations, the total energy of the system is constructed

as a functional of nucleon densities. In the DRHBc theory, by using the Bogoliubov transformation, the MF and pairing correlations are treated self-consistently [77,80]. The equation of motion for nucleons is the deformed RHB equation [120] and reads

$$\begin{pmatrix} h_D - \lambda_\tau & \Delta \\ -\Delta^* & -h_D^* + \lambda_\tau \end{pmatrix} \begin{pmatrix} U_k \\ V_k \end{pmatrix} = E_k \begin{pmatrix} U_k \\ V_k \end{pmatrix}, \tag{1}$$

where λ_τ $(\tau = n, p)$ is the Fermi energy. $(U_k, V_k)^T$ is the quasiparticle wave function with energy E_k and is expanded in terms of the Dirac WS basis:

$$U_k(\boldsymbol{r}s) = \sum_{n\kappa} u^{(m)}_{k,(n\kappa)} \varphi_{n\kappa m}(\boldsymbol{r}s),$$
$$V_k(\boldsymbol{r}s) = \sum_{n\kappa} v^{(m)}_{k,(n\kappa)} \bar{\varphi}_{n\kappa m}(\boldsymbol{r}s). \tag{2}$$

The Dirac WS basis is obtained by solving the Dirac equation in r space with the spherical WS scalar and vector potentials [71,121], and the basis function reads

$$\varphi_{n\kappa m}(\boldsymbol{r}s) = \frac{1}{r} \begin{pmatrix} iG_{n\kappa}(r)\mathcal{Y}^l_{jm}(\Omega s) \\ -F_{n\kappa}(r)\mathcal{Y}^{\tilde{l}}_{jm}(\Omega s) \end{pmatrix}, \tag{3}$$

where $\mathcal{Y}^l_{jm}(\Omega s)$ is the spin spherical harmonics with the total angular momentum j, orbital angular momentum l, and the projection m of the total angular momentum on the symmetry axis. $G_{n\kappa}(r)/r$ and $F_{n\kappa}(r)/r$ are radial wave functions for the upper and lower components of the Dirac spinor with the radial quantum number n and the relativistic quantum number $\kappa = (-)^{j+l+1/2}(j + 1/2)$. $\bar{\varphi}_{n\kappa m}(\boldsymbol{r}s)$ is the time reversal partner of $\varphi_{n\kappa m}(\boldsymbol{r}s)$.

The Dirac Hamiltonian reads

$$h_D = \boldsymbol{\alpha} \cdot \boldsymbol{p} + V(\boldsymbol{r}) + \beta[M + S(\boldsymbol{r})], \tag{4}$$

where $S(\boldsymbol{r})$ and $V(\boldsymbol{r})$ are the scalar and the vector potentials and read

$$S(\boldsymbol{r}) = \alpha_S \rho_S + \beta_S \rho_S^2 + \gamma_S \rho_S^3 + \delta_S \Delta\rho_S, \tag{5}$$

$$V(\boldsymbol{r}) = \alpha_V \rho_V + \gamma_V \rho_V^3 + \delta_V \Delta\rho_V + e\frac{1-\tau_3}{2}A^0 + \alpha_{TV}\tau_3\rho_3 + \delta_{TV}\tau_3\Delta\rho_3. \tag{6}$$

The densities read

$$\rho_S(\boldsymbol{r}) = \sum_{k>0} V_k^\dagger(\boldsymbol{r})\gamma_0 V_k(\boldsymbol{r}),$$
$$\rho_V(\boldsymbol{r}) = \sum_{k>0} V_k^\dagger(\boldsymbol{r}) V_k(\boldsymbol{r}),$$
$$\rho_3(\boldsymbol{r}) = \sum_{k>0} V_k^\dagger(\boldsymbol{r})\tau_3 V_k(\boldsymbol{r}). \tag{7}$$

The pairing potential is written as

$$\Delta(\boldsymbol{r}_1, \boldsymbol{r}_2) = V^{pp}(\boldsymbol{r}_1, \boldsymbol{r}_2)\kappa(\boldsymbol{r}_1, \boldsymbol{r}_2), \tag{8}$$

where $\kappa(\boldsymbol{r}_1, \boldsymbol{r}_2)$ is the pairing tensor [32,122], and a density-dependent zero-range force,

$$V^{pp}(\boldsymbol{r}_1, \boldsymbol{r}_2) = \frac{1}{2}V_0(1 - \hat{P}^\sigma)\delta(\boldsymbol{r}_1 - \boldsymbol{r}_2)\left[1 - \left(\frac{\rho(\boldsymbol{r}_1)}{\rho_{\rm sat}}\right)\right], \tag{9}$$

is used in the present work.

In the intrinsic frame, for axially symmetric and spatial reflection symmetric nuclei, the densities and potentials are expanded in terms of the Legendre polynomials,

$$f(\boldsymbol{r}) = \sum_\lambda f_\lambda(r) P_\lambda(\cos\theta), \quad \lambda = 0, 2, 4, \ldots, \tag{10}$$

with

$$f_\lambda(r) = \frac{2\lambda + 1}{4\pi} \int d\Omega f(\boldsymbol{r}) P_\lambda(\cos\theta). \tag{11}$$

After getting the wave functions by solving the RHB equation, the total energy of the system can be obtained, and more details can be found in Ref. [106].

B. Angular momentum projection

Due to the breaking of spherical symmetry by the axially deformed MF potential in the intrinsic frame, the wave function $|\Phi(\beta_2)\rangle$ with a certain quadrupole deformation parameter β_2 is not an eigenvector of angular momentum operators $\hat{J}_z$ and $\hat{J}^2$. The projected ground state and low-lying excited states with good angular momentum can be constructed by performing the AMP on $|\Phi(\beta_2)\rangle$ given by DRHBc calculations with the quadrupole deformation constraint [97] and read [32]

$$\left|\Psi^{JM}_\alpha(\beta_2)\right\rangle = \sum_K f^{JK}_\alpha \hat{P}^J_{MK}|\Phi(\beta_2)\rangle, \tag{12}$$

where f^{JK} is a coefficient and the angular momentum projection operator reads

$$\hat{P}^J_{MK} = \frac{2J+1}{8\pi^2} \int d\Omega D^{J*}_{MK}(\Omega)\hat{R}(\Omega), \tag{13}$$

with the Euler angles $\Omega \equiv (\phi, \theta, \varphi)$, the Wigner function $D^J_{MK}(\Omega)$, and the rotational operator $\hat{R}(\Omega) = e^{-i\phi\hat{J}_z}e^{-i\theta\hat{J}_y}e^{-i\varphi\hat{J}_z}$. The energy E^J and f^{JK} of a projected state can be calculated by solving the Hill-Wheeler equation [32]:

$$\sum_K f^{JK}_\alpha \left[\left\langle\Phi(\beta_2)|\hat{H}\hat{P}^J_{MK}|\Phi(\beta_2)\right\rangle - E^J_\alpha\left\langle\Phi(\beta_2)|\hat{P}^J_{MK}|\Phi(\beta_2)\right\rangle\right] = 0. \tag{14}$$

For axially deformed nuclei, the calculation of E^J and f^{JK} can be simplified because $\hat{J}_z|\Phi(\beta_2)\rangle = 0$. The integration over ϕ and φ can be calculated analytically. Using the properties of the projection operator and spatial reflection symmetry, one can deduce $K = 0$ and f^{JK} can be replaced by f^J. E^J and f^J are calculated as [123]

$$E^J = \frac{\langle\Phi(\beta_2)|\hat{H}\hat{P}^J_{00}|\Phi(\beta_2)\rangle}{\langle\Phi(\beta_2)|\hat{P}^J_{00}|\Phi(\beta_2)\rangle},$$
$$f^J = \frac{1}{\sqrt{\langle\Phi(\beta_2)|\hat{P}^J_{00}|\Phi(\beta_2)\rangle}}. \tag{15}$$

The normal overlap kernel $\mathcal{N}^J(\beta_2)$ and the Hamiltonian overlap kernel $\mathcal{H}^J(\beta_2)$ can obtained by using the formulas in [111].

For the calculation of the normal overlap kernel and Hamiltonian overlap kernel, the generalized Wick's theorem is used [124–127], and in this work we use the formulas and notation

given in Ref. [50]. In practical calculations, the wave functions of single-particle states in the canonical basis with tiny occupation probabilities v^2 have negligible contribution to kernels. Therefore a truncation ξ on the occupation probability is introduced, which can reduce the numerical computational efforts [50,124] effectively.

The main ingredient for calculating the normal overlap defined as $n(\beta_2;\theta) \equiv \langle\Phi(\beta_2)|\hat{R}(\theta)|\Phi(\beta_2)\rangle$ with $\hat{R}(\theta) \equiv e^{-i\theta\hat{J}_y}$ is the rotational matrix, and the matrix elements can be easily obtained:

$$\begin{aligned} R_{kk'} &= \langle\phi_k|\hat{R}(\theta)|\phi_{k'}\rangle \\ &= \sum_{n\kappa}\sum_{n'\kappa'} c^k_{n\kappa m} c^{k'}_{n'\kappa' m'} \delta_{jj'}\delta_{ll'} d^{j'}_{mm'}(\theta). \end{aligned} \tag{16}$$

We notice that it is simpler to calculate the rotation matrix elements in the Dirac WS basis than in the HO basis shown in Refs. [50,111] because the Dirac WS basis functions are eigenvectors of angular momentum operators and

$$\langle n\kappa m|\hat{R}(\theta)|n'\kappa' m'\rangle = \delta_{jj'}\delta_{ll'} d^{j'}_{mm'}(\theta). \tag{17}$$

We follow the procedures given in Refs. [50,111] to calculate the Hamiltonian overlap kernel. For each rotational angle, the energy density $\mathcal{E}(\beta_2;\theta)$ has the similar structure with that in the MF level and is a functional of the mixed density $\rho(\boldsymbol{r};\beta_2;\theta)$ and pairing density $\kappa(\boldsymbol{r};\beta_2;\theta)$ in r space. It should be mentioned that in AMP calculations, the rotation operation breaks the time reversal symmetry, and therefore the spatial components of the currents have contribution to the total energy. In coordinate space, the mixed densities and currents are

$$\begin{aligned} \rho_V(\boldsymbol{r};\beta_2;\theta) &= \sum_{i,j} \bar{\phi}_i(\boldsymbol{r};\beta_2)\rho_{ji}(\theta)\phi_j(\boldsymbol{r};\beta_2), \\ \rho_3(\boldsymbol{r};\beta_2;\theta_2) &= \sum_{i,j} \bar{\phi}_i(\boldsymbol{r};\beta_2)\tau_3\rho_{ji}(\theta)\phi_j(\boldsymbol{r};\beta_2), \\ j^\mu(\boldsymbol{r};\beta_2;\theta) &= \sum_{i,j} \bar{\phi}_i(\boldsymbol{r};\beta_2)\gamma^\mu\rho_{ji}(\theta)\phi_j(\boldsymbol{r};\beta_2), \end{aligned} \tag{18}$$

where $\phi(\boldsymbol{r})$ and $\bar{\phi}(\boldsymbol{r})$ are the single-particle wave function and its time reversal partner. $\rho(\theta)$ is the mixed density matrix in the canonical basis for each rotation angle and can be calculated after obtaining the rotational matrix. More details can be found in Ref. [50].

In the DRHBc theory, the intrinsic densities are axially symmetric along the z axis and are spatial-reflection symmetric. Therefore the density is expressed as a linear combination of the Legendre polynomials [cf. Eq. (10)]. For the mixed densities, the rotational invariance along the z axis is broken but kept along the y axis and the spatial reflection symmetry is also held. For the currents, the symmetry of the time component is the same as that of the mixed densities, and the spatial components are spatial-reflection asymmetric. So in the DRHBc+AMP approach, we expand the mixed densities and currents in terms of the spherical harmonics,

$$f(r,\vartheta,\omega) = \sum_{l=0}^{\infty}\sum_{m=-l}^{m=l} a_{lm}(r)Y_{lm}(\vartheta,\omega), \tag{19}$$

where

$$a_{lm}(r) = \int_0^{2\pi} d\omega \int_0^{\pi} \sin\vartheta d\vartheta Y^*_{lm}(\vartheta,\omega) f(r,\vartheta,\omega). \tag{20}$$

For the mixed scalar density and vector density, we have

$$\rho(\boldsymbol{r}) = \sum_l \sum_{m=-l}^{m=l} \rho_{lm}(r)Y_{lm}(\vartheta,\omega),\ l = 0,2,4,\ldots, \tag{21}$$

and $\rho_{l-m}(r) = (-1)^m\rho_{lm}(r)$.

For the spatial components of the mixed currents,

$$\vec{j}(\boldsymbol{r}) = \sum_l \sum_{m=-l}^{m=l} \vec{j}_{lm}(r)Y_{lm}(\vartheta,\omega),\ l = 1,3,5,\ldots, \tag{22}$$

with $j_{x(z),l-m}(r) = (-1)^m j_{x(z),lm}(r)$ and $j_{y,l-m}(r) = (-1)^{m+1} j_{y,lm}(r)$. The details about how to calculate the mixed densities and currents in coordinate space within the framework of the DRHBc+AMP are given in Appendix.

After the calculation of the mixed densities and currents, the interaction part of $\mathcal{E}(\beta_2;\theta)$ can be obtained. The Coulomb part of the mixed energy density is calculated as

$$\mathcal{E}_{\rm em}(\boldsymbol{r};\theta) = \frac{e^2}{8\pi}\rho_p(\boldsymbol{r};\theta)\int d^3\boldsymbol{r}'\frac{\rho_p(\boldsymbol{r}';\theta)}{|\boldsymbol{r}-\boldsymbol{r}'|}. \tag{23}$$

As what is usually done, the exchange term of Coulomb energy is neglected. By expanding $\frac{1}{|\boldsymbol{r}-\boldsymbol{r}'|}$ and mixed proton density in terms of the spherical harmonics, one can get the Coulomb energy. The pairing part of the mixed energy density is given by

$$\mathcal{E}_{\rm pair}(\boldsymbol{r};\theta) = -\sum_\tau \frac{V_\tau(\boldsymbol{r};\theta)}{4}\kappa^*_\tau(\boldsymbol{r};\theta)\kappa_\tau(\boldsymbol{r};\theta), \tag{24}$$

and the mixed densities are used when calculating $V_\tau(\boldsymbol{r};\theta)$. The correction energy of the center-of-mass spurious motion in the AMP is taken to be the same as that in MF calculations. To consider the correction from the breaking of particle numbers, following the procedures in Ref. [51], a term with the form of $-\lambda_p[Z(\boldsymbol{r};\theta)-Z_0]-\lambda_n[N(\boldsymbol{r};\theta)-N_0]$ is added into the mixed energy density. Z_0 and N_0 are the number of protons and neutrons for a given nucleus, and λ_p (λ_n) is the Fermi energy for protons (neutrons) of the intrinsic state $|\Phi(\beta_2)\rangle$. $Z(\boldsymbol{r};\theta)$ and $N(\boldsymbol{r};\theta)$ are the mixed vector densities in r space for protons and neutrons, respectively. After the calculation of the mixed energy density, the solution of Eq. (15) can be gotten.

In this work we study even-even nuclei and focus on excited states with positive parity. The reduced transition probability, the spectroscopic quadrupole moment, and dimensionless quadrupole deformation parameter β^s are calculated by using the formulas given in Refs. [128] and [129].

III. NUMERICAL CHECKS

In this section we check the numerical parameters involved in DRHBc+AMP calculations in detail. The whole numerical process includes two parts: the MF (i.e., DRHBc) and AMP calculations. For MF calculations with the point-coupling and meson-exchange density functionals, the numerical details

have been presented in Refs. [106] and [94], respectively. In this work, most of the parameters are taken to be the same as those given in Ref. [106], and here we reexamine the energy cutoff in the Fermi sea of the Dirac WS basis in order to save computation time. For AMP calculations, we examine the accuracy of the integral for the calculations of the normal overlap and the expansion of the spherical harmonics in Eq. (19). Two truncation parameters are introduced to determine the number of the single-particle levels (SPLs) used in AMP calculations, and the convergences of energies of projected states and reduced transition probability with respect to these two cut-off parameters are shown.

A. MF calculations

In the particle-hole channel, the density functional PC-F1 [130] is adopted to compare our results obtained from DRHBc+AMP calculations with those in Ref. [50]. The box size $R_{\rm box}$ used to generate the Dirac WS basis can be approximated by $4r_0A^{1/3}$, with $r_0 = 1.2$ fm for light nuclei [94], and is taken to be 20 fm for other nuclei. The mesh size Δr is equal to 0.1 fm. The order of the Legendre expansion is up to 6 in Eq. (10) [131]. The angular momentum cutoff is taken to be $21/2\hbar$. By adjusting pairing gaps around ^{38}Mg (three-point formula), the pairing strength V_0 is taken to be 240 MeV fm^3 and 325 MeV fm^3 for neutrons and protons, respectively, which slightly differs from those values used in Ref. [132] with a density-independent zero-range pairing force. For the pairing window, the cut-off energy is taken to be 60 MeV in the quasiparticle space [94]. In the DRHBc theory, an energy cutoff $E_{\rm cut}$ is introduced to determine the number of basis states in the Fermi sea, and the number of basis states in the Dirac sea is taken to be the same as that in the Fermi sea. For the nuclear mass table calculation with the density functional PC-PK1 [106], the energy cutoff for positive energy states is $E_{\rm cut} = 300$ MeV for the Dirac WS basis, which can provide an accuracy about 0.001% for global calculations of the total energy. If we use this cut-off energy in DRHBc+AMP calculations with PC-F1, it takes too many CPU hours due to the very large space size of the single particle basis. Therefore we recheck the relative accuracy of the bulk properties with respect to $E_{\rm cut}$ for calculations with the density functional PC-F1 and find a relatively small and reasonable value of $E_{\rm cut}$ which can ensure the precision, as well as save the computation time, especially for AMP calculations.

For ^{38}Mg, two energy minima are found in the potential energy curve and the ground state has a prolate shape. In Fig. 1 we show the calculated bulk properties of ^{38}Mg in the ground state with prolate shape and in the oblate minimum by using the DRHBc theory with the density functional PC-F1. From this figure it is obvious that with the increase of $E_{\rm cut}$, the total energy, rms matter radius, and deformation parameter all converge well at $E_{\rm cut} = 200$ MeV. The difference of total energies between $E_{\rm cut} = 200$ MeV and $E_{\rm cut} = 220$ MeV is about 0.01 MeV. This means that when $E_{\rm cut} = 200$ MeV the relative accuracy of binding energy is less than 0.005%, which is accurate enough for the study of ground-state properties. The relative accuracies of radius and deformation parameter

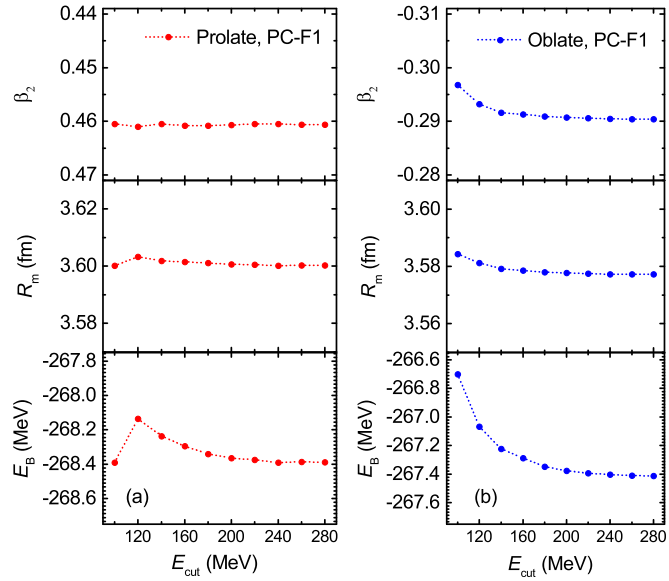

FIG. 1. The total energy $E_{\rm B}$, rms matter radius R_m, and quadrupole deformation parameter β_2 of the ground state (a) and oblate isomer (b) for ^{38}Mg as a function of $E_{\rm cut}$ in DRHBc calculations with PC-F1.

are close to 0.1%. Therefore in the following calculations, $E_{\rm cut} = 200$ MeV is adopted.

B. AMP calculations

For axially deformed nuclei, the normal overlap can be analytically calculated by using the Gaussian overlap approximation (GOA) [37,133],

$$n_{\rm GOA}(\beta_2;\theta) = \exp\left[-\frac{1}{2}\langle\hat{J}_y^2\rangle\sin^2\theta\right], \tag{25}$$

with $\langle\hat{J}_y^2\rangle = \langle\Phi(\beta_2)|\hat{J}_y^2|\Phi(\beta_2)\rangle$. It has been checked in several works [37,50,111,133] that the GOA is a good approximation for the normal overlap for both small and large deformation parameters and can be used to examine the result of the normal overlap in AMP calculations. In Fig. 2, we show the $n(\beta_2;\theta)$ values calculated numerically by using the AMP and those obtained under the GOA for ^{24}Mg with β_2 constrained to be 0.9. It can be seen that the calculated values of $n(\beta_2;\theta)$ are in good agreement with those obtained under the GOA, meaning that our calculations for the normal overlap are reliable. For the spherical case ($\beta_2 = 0$), the calculated values of $n(\beta_2;\theta)$ are equal to 1 due to the rotational invariance. It also should be mentioned that the GOA is only valid for the normal overlap but not for the rotational energy correction for weakly bound deformed systems [128,133], which can be well approximated by using the topologically corrected GOA [134].

For the Hamiltonian and normal overlap kernels, the one-dimensional integral over θ is calculated by using the Gaussian-Legendre quadrature, and the number of the mesh points in the interval $[0, \pi]$ is n_θ. We have checked that when the number of the mesh point of the Euler angle θ in the interval $[0, \pi]$ satisfies $n_\theta \geqslant 10$, the relative accuracies of $E^{J=0}$ and $B(E2, 2^+ \to 0^+)$ are about 0.0001%. In this work,

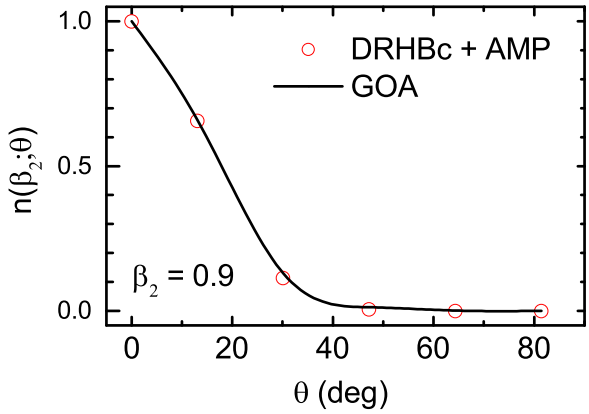

FIG. 2. Normal overlap of ^{24}Mg with the quadrupole deformation parameter of 0.9 from the AMP (black circles) and GOA (red lines) calculations as a function of θ with PC-F1.

$n_\theta = 12$ is used. This conclusion is consistent with that given in Ref. [50].

The ingredients for the mixed energy density are the mixed densities and currents, which are expanded in terms of the spherical harmonics [cf. Eq. (19)]. The convergence with respect to the maximum expansion orders l_ρ in Eq. (21) and l_j in Eq. (22) for mixed densities and currents should be analyzed. In the left panel of Fig. 3, the calculated values of $E^{J=0}$ and $B(E2, 2^+ \to 0^+)$ for ^{24}Mg with $\beta_2 = 0.55$ are plotted as a function of l_ρ with l_j fixed to be 7. The calculated values of $B(E2, 2^+ \to 0^+)$ are almost unchanged with l_ρ. We find that to achieve a precision of 0.01% for $E^{J=0}$, the maximum expansion order l_ρ should fulfill $l_\rho \geqslant 6$. With l_ρ fixed to be 6, the calculated values of $E^{J=0}$ and $B(E2, 2^+ \to 0^+)$ are plotted as a function of l_j in the right panel of Fig. 3. One can see that when $l_j = 3$ and $l_j = 5$, the calculation of $E^{J=0}$ and $B(E2, 2^+ \to 0^+)$ can reach a relative accuracy of 0.01% and 0.001%, respectively. The time consumption of the calculations of the currents is much heavier than that for the mixed densities, and the relative accuracy with $l_j = 3$ is good enough

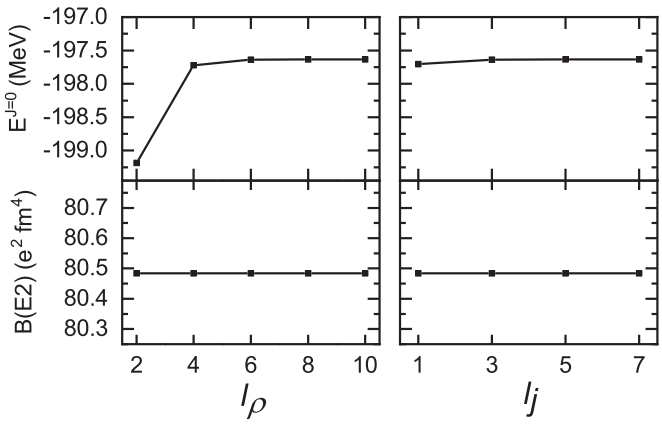

FIG. 3. $E^{J=0}$ and $B(E2, 2^+ \to 0^+)$ obtained from angular momentum projections on the intrinsic state with $\beta_2 = 0.55$ for ^{24}Mg as a function of l_ρ (the left panel, $l_j = 7$) and l_j (the right panel, $l_\rho = 6$).

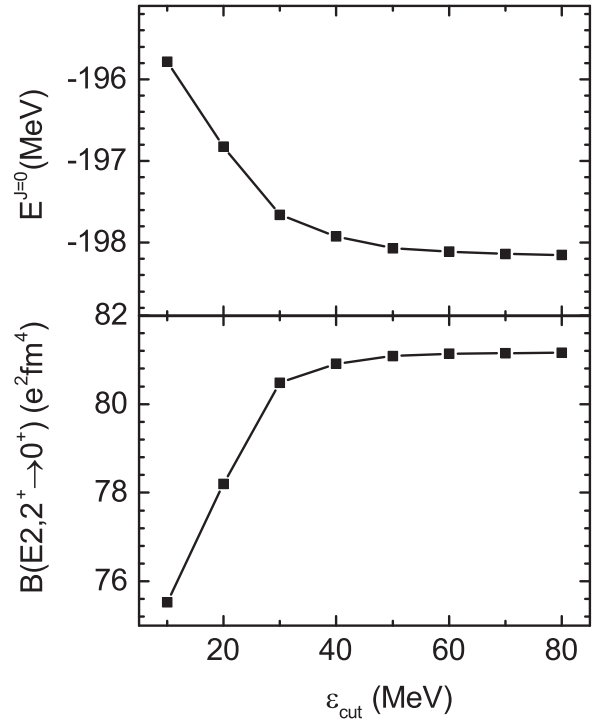

FIG. 4. $E^{J=0}$ and $B(E2, 2^+ \to 0^+)$ obtained from angular momentum projections on the intrinsic state with $\beta_2 = 0.55$ for ^{24}Mg as a function of ϵ_{cut}.

for the spectroscopic study. Therefore for later calculations we choose $l_j = 3$ and $l_\rho = 6$.

For the calculation of the rotational matrix, as mentioned in Sec. II B, we introduce a truncation ξ on the occupation probability of SPLs in the canonical basis to determine the dimension of this matrix. It has been shown in Ref. [50] that $E^{J=0}$ and reduced transition probability converge well at $\xi = 10^{-7}$ or 10^{-8}. This also holds in our calculations. But when the calculated pairing energy equals zero or the pairing strength is taken to be zero, the SPLs below or above the Fermi level (λ_τ) are fully occupied or empty, respectively. The truncation on the occupation probability is no longer suitable in this case. Therefore we also introduce a cut-off energy on the single-particle energy (SPE) in the canonical basis to determine the total number of SPLs for AMP calculations, i.e., SPLs with the energy larger than $\lambda_\tau + \epsilon_{\text{cut}}$ are neglected for neutrons ($\tau = 1$) and protons ($\tau = -1$). In Fig. 4, $E^{J=0}$ and $B(E2, 2^+ \to 0^+)$ are shown as a function of the cut-off energy ϵ_{cut}. The relative accuracies of $E^{J=0}$ and $B(E2, 2^+ \to 0^+)$ are about 0.01% when $\epsilon_{\text{cut}} = 50$ MeV. In practical calculations, those SPLs with $v^2 > 10^{-7}$ or SPE smaller than $\lambda_\tau + 50$ MeV are used.

Now we summarize the parameters involved in DRHBc+AMP calculations. The energy cutoff E_{cut} for positive energy states in the Dirac WS basis is 200 MeV in MF calculations. The number of mesh points in the Gaussian-Legendre quadrature for the calculation of the normal overlap kernel and Hamiltonian overlap kernel is $n_\theta = 12$ in the interval $[0, \pi]$. For the mixed density and currents expanded in terms of the spherical harmonics,

TABLE I. Excitation energies and $B(E2)$ from DRHBc+AMP (Th. I) and MDC-RHB+AMP (Th. II) calculations for ^{24}Mg with $\beta_2 = 0.55$ and $\beta_2 = 0.65$.

	$\beta_2 = 0.55$		$\beta_2 = 0.65$	
	Th. I	Th. II	Th. I	Th. II
$E(2^+)$ (MeV)	1.009	1.006	1.149	1.128
$E(4^+)$ (MeV)	3.553	3.556	3.956	3.890
$E(6^+)$ (MeV)	8.024	8.074	8.627	8.542
$B(E2, 2^+ \to 0^+)$ (e^2 fm^4)	81.083	81.214	110.606	110.750
$B(E2, 4^+ \to 2^+)$ (e^2 fm^4)	118.126	118.752	161.459	162.156
$B(E2, 6^+ \to 4^+)$ (e^2 fm^4)	135.674	136.939	185.670	186.912

the maximum orders are $l_\rho = 6$ and $l_j = 3$, respectively. For determining the number of SPLs, the truncation of the occupation probability is $\xi = 10^{-7}$ and $\epsilon_{\rm cut} = 50$ MeV for SPE.

To check this newly developed method further, the DRHBc+AMP method is applied to stable nuclei and the calculated results are compared with those from MDC-RHB+AMP calculations [117]. In Table I, we show the excitation energies of 2^+, 4^+, and 6^+ states and $B(E2)$ values obtained in DRHBc+AMP and MDC-RHB+AMP calculations for ^{24}Mg with the quadrupole deformation parameter constrained to be 0.55 and 0.65. The density functional PC-F1 is used in both methods. In MDC-RHB+AMP calculations, the number of oscillator shells is taken to be 14 and the number of mesh points of the Euler angle θ in the interval $[0, \pi]$ equals 12. For both the excitation energies and $B(E2)$ values, the relative differences between these two methods are around 1%. From this comparison one can conclude that for well-bound nuclei, the low-lying excited spectra and $B(E2)$ values from DRHBc+AMP calculations are well consistent with the results from the MDC-RHB+AMP method.

IV. LOW-LYING EXCITED STATES OF ^{36,38,40}Mg WITH DRHBc+AMP

In this section we will use the DRHBc+AMP approach to study the neutron-rich Mg isotopes ^{36,38,40}Mg. The spectra of these nuclei are interesting topics, both theoretically and experimentally in recent years, which are closely related to the weakening of spherical shells, the disappearance of magic numbers, and the island of inversion. The low-lying spectra of ^{36,38,40}Mg have also been established [135,136], and the recent experimental results of ^{40}Mg indicates the quenching of the shell closure at $N = 28$ [136]. There are many systematic theoretical investigations on these nuclei, including MF calculations [94,96,137], the shell model calculations [138,139], BMF calculations with the Skyrme density functional [17,124] and Gogny force [49,128,140,141], and beyond RMF calculations [132,142].

A. Bulk properties

Before exploring the excitation of these nuclei, we show the ground-state properties in MF level by using the DRHBc theory. The calculated bulk properties of ^{36}Mg, ^{38}Mg, and ^{40}Mg are listed in Table II. In DRHBc calculations with the density functional PC-F1, the quadrupole deformation parameters of the ground states of ^{36}Mg, ^{38}Mg, and ^{40}Mg are 0.45, 0.49, and 0.48, respectively. The calculated rms matter radii (R_m) of ^{36}Mg and ^{38}Mg are 3.49 fm and 3.62 fm, which are well consistent with the experimental values [143], 3.49 ± 0.01 fm and 3.60 ± 0.04 fm, which are extracted from the measurements of total cross sections [144]. The calculated value of R_m for ^{40}Mg is 3.70 fm. The two-neutron separation energy with considering the correction from the AMP of ^{38}Mg is 3.06 MeV, which agrees with the experimental value, 2.45(85) MeV [145,146], and that of ^{40}Mg is 2.74 MeV, which is larger than the experimental values, 1.87(71) MeV in AME2016 [145] and 0.65(0.71) MeV in AME2020 [146]. In Fig. 5 we show the SPLs with -12 MeV $< \epsilon_{\rm can} < 1$ MeV in the canonical basis for ^{36,38,40}Mg in DRHBc calculations. It should be noted that near the neutron Fermi energy λ_n, the $1/2^-$ and $3/2^-$ levels contain p-wave components and the $5/2^-$ level is totally dominated by f-wave components. Around λ_n, SPLs are all fully occupied, with $v^2 = 1$ for ^{36,40}Mg and partially occupied for ^{38}Mg, meaning the enhancement of pairing in ^{38}Mg. ^{37}Mg is a p-wave halo nucleus, and the valence neutron is unpaired [83,147]. The configuration of the two valence neutrons for ^{38}Mg also includes p-wave components and is mainly the mixing of $2p_{1/2}$ and $1f_{7/2}$ with occupation numbers of 0.72 and 1.18. For ^{40}Mg,

TABLE II. Ground-state properties from DRHBc calculations with PC-F1 and energies of the projected 0^+ state of ^{36}Mg, ^{38}Mg, and ^{40}Mg. For each nucleus, we show the neutron, proton, and total quadrupole deformation parameters (β_n, β_p, β_2), neutron, proton, and total rms matter radii (R_n, R_p, R_t), the correction energy ($E_{\rm c.m.}$) of center-of-mass spurious motion, the total energy ($E_{\rm B}$), and the energy ($E^{J=0}$) of the projected 0^+ state.

	^{36}Mg	^{38}Mg	^{40}Mg
β_n	0.4568	0.5150	0.5006
β_p	0.4331	0.4339	0.4197
β_2	0.4489	0.4894	0.4764
R_n (fm)	3.6593	3.8191	3.9066
R_p (fm)	3.1276	3.1568	3.1815
R_t (fm)	3.4911	3.6230	3.7040
$E_{\rm c.m.}$ (MeV)	−9.3127	−9.1469	−8.9914
$E_{\rm B}$ (MeV)	−265.3905	−267.9706	−270.9131
$E^{J=0}$ (MeV)	−268.0396	−271.1044	−273.8405

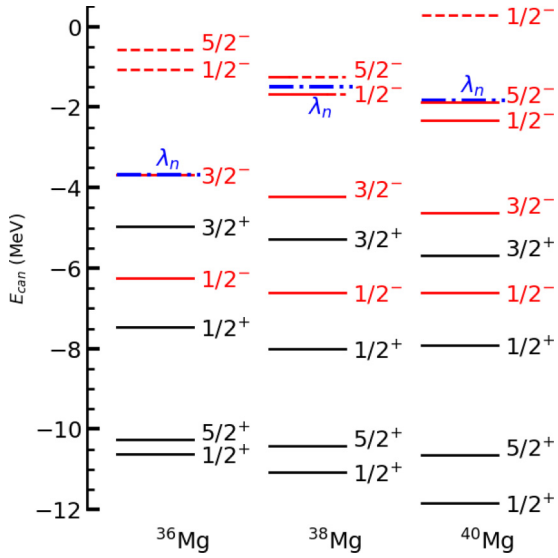

FIG. 5. SPLs of neutrons around the Fermi energy (λ_n) of ^{36}Mg, ^{38}Mg, and ^{40}Mg in the canonical basis. The length of the solid line is proportional to the occupation probability v^2 of each level labeled by Ω^π, where Ω and π are the projection of total angular momentum on the symmetry axis in the intrinsic frame and parity. Red and black lines represent levels with $\pi = -$ and $\pi = +$, respectively.

the fully occupied levels $5/2^-$ and $1/2^-$ near the Fermi energy are close to each other. It has been shown in Refs. [143,148] that there is a cross between the $5/2^-$ and $1/2^-$ orbitals when $\beta_2 \approx 0.5$ around the neutron Fermi energy. Because of the near degeneracy of $(1/2^-, 5/2^-)$, it is reasonable to regard ^{40}Mg as a "^{36}Mg $+4n$" system instead of "^{38}Mg $+2n$" from the point of view of the structure of SPLs. The four valence neutrons are dominated by p- and f-wave components with the occupation numbers of 1.2 and 2.8, respectively. In conclusion, the configurations of the valence neutrons for ^{38}Mg and ^{40}Mg all have p-wave components with considerable occupation, but they are not halo nuclei because the valence neutrons are not weakly bound with calculated two-neutron separation energies larger than 2 MeV. Note that the study in Ref. [83] shows that ^{40}Mg is a two-neutron halo nucleus, which is contrary to the conclusion drawn in our DRHBc calculations.

B. Ground-state rotational bands of ^{36,38,40}Mg

In this study, the low-lying excited spectrum is obtained by performing the AMP on the deformed ground state obtained from DRHBc calculations with the density functional PC-F1, i.e., for each nucleus the same MF wave function is used to get the projected states. For ^{36,38,40}Mg, the calculated values of the excitation energy $E(J^+)$, spectroscopic quadrupole moment $Q^{(s)}(J^+)$, and reduced transition probability $B(E2)$ are summarized in Table III. As shown in Refs. [128,132], for well-deformed nuclei ^{36,38,40}Mg the differences of excitation energies between AMP and AMP+GCM calculations are relatively small. Therefore, for these three nuclei, we can directly compare our results from DRHBc+AMP calculations with those with GCM. In Fig. 6 the calculated ground-state

TABLE III. Calculated excitation energy $E(J^+)$, spectroscopic quadrupole moment $Q^{(s)}(J^+)$, and reduced transition probabilities $B(E2)$ for ^{36,38,40}Mg with PC-F1.

	^{36}Mg	^{38}Mg	^{40}Mg
$E(2^+)$ (MeV)	0.46	0.66	0.53
$E(4^+)$ (MeV)	1.61	2.15	1.82
$E(6^+)$ (MeV)	3.65	4.44	3.94
$Q^{(s)}(2^+)$ (e fm^2)	−18.21	−18.96	−18.99
$Q^{(s)}(4^+)$ (e fm^2)	−23.22	−24.19	−24.26
$Q^{(s)}(6^+)$ (e fm^2)	−25.64	−26.73	−26.83
$B(E2, 2^+ \to 0^+)$ (e^2 fm^4)	80.91	87.66	87.89
$B(E2, 4^+ \to 2^+)$ (e^2 fm^4)	117.39	127.01	126.88
$B(E2, 6^+ \to 4^+)$ (e^2 fm^4)	133.06	143.29	142.57

bands of ^{36}Mg, ^{38}Mg, and ^{40}Mg are shown and compared with the experimental values taken from Ref. [136]. $B(E2\downarrow)$ values obtained from DRHBc+AMP calculations are also given. The overall trends of spectra from DRHBc+AMP calculations are consistent with the results obtained from the RMF+1DAMP+GCM calculations with PC-F1 [132], in which the HO basis is used and close to those shown in Ref. [141]. The excitation energies from BMF calculations with Gogny force [128] are higher than these results in this work. The ground-state band of ^{40}Mg from our calculations is also close to that of recent Monte Carlo shell model (MCSM) calculations [139]. The calculated excitation energies of the 2^+ and 4^+ states for ^{36}Mg are slightly smaller than the experimental values. The 2^+ states of ^{38}Mg and ^{40}Mg are very close to the experimental values. Generally speaking, the DRHBc+AMP calculations reproduce the experimental low-lying spectra of ^{36,38,40}Mg reasonably well. All the BMF calculations mentioned above support that the shell closure

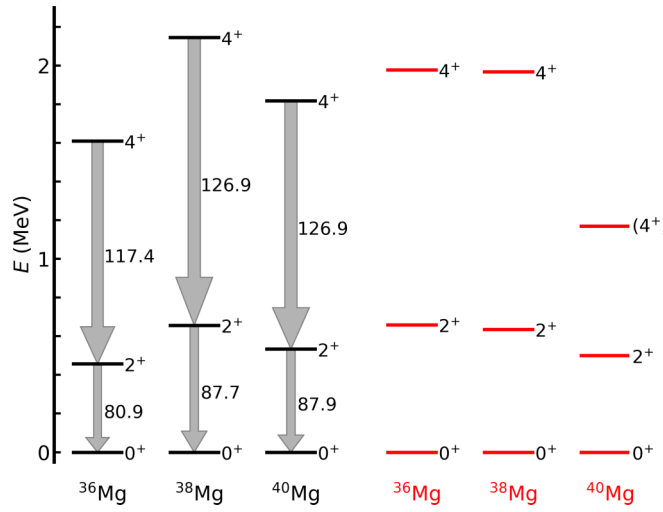

FIG. 6. The ground-state rotational bands and values of $B(E2)$ of ^{36}Mg, ^{38}Mg, and ^{40}Mg. Black lines and gray arrows represent the results from DRHBc+AMP calculations, and red lines show the experimental data taken from Ref. [136]. Transitions between two states are represented by arrows, and the width of each arrow is proportional to reduced transition probability.

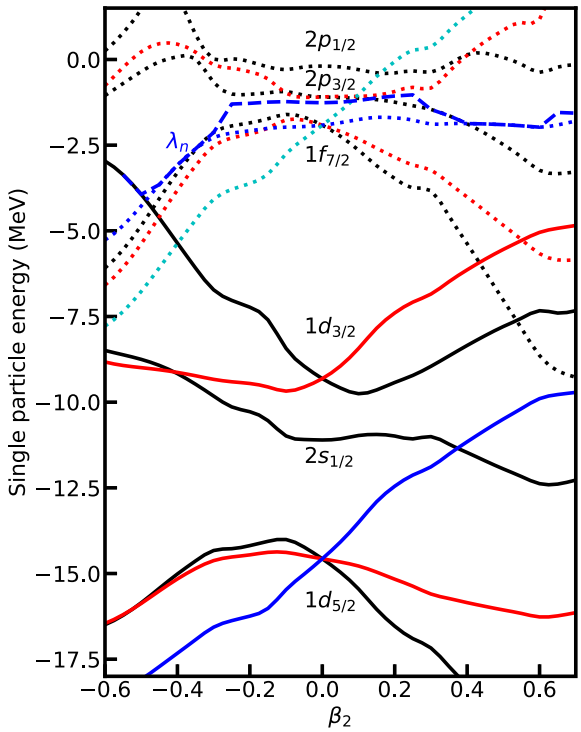

FIG. 7. SPLs of neutrons for ^{40}Mg in the canonical basis. Solid and dotted lines represent levels with $\pi = -$ and $\pi = +$, respectively. The Fermi energy λ_n is shown by the dashed line. Black, red, blue, and cyan colors represent levels with Ω of 1/2, 3/2, 5/2, and 7/2, respectively.

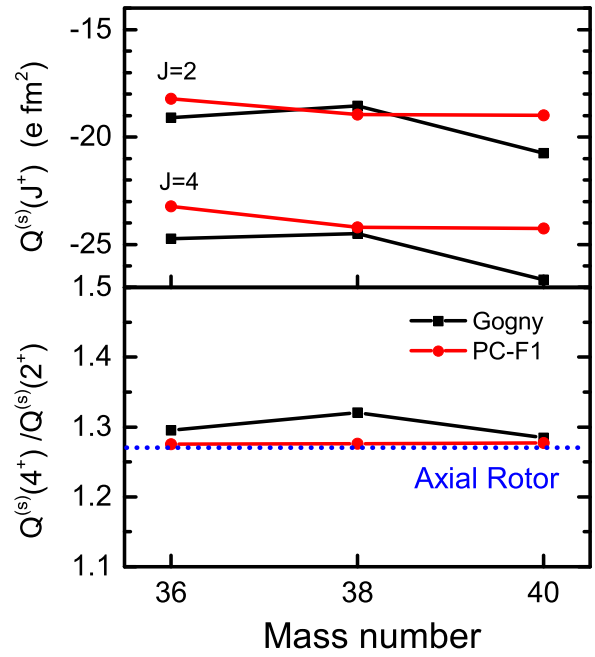

FIG. 8. Spectroscopic quadrupole moments $Q^{(s)}$ of the 2^+ and 4^+ states (the top panel) and the ratios $Q^{(s)}(4^+)/Q^{(s)}(2^+)$ (the bottom panel) for ^{36,38,40}Mg.

at $N = 28$ is quenched and ^{40}Mg has a prolate shape as a consequence of the very small value of the excitation energy of the 2^+ state.

The disappearance of the shell $N = 28$ in ^{40}Mg can be also indicated by the evolution of the SPLs, which are shown in Fig. 7. When $\beta_2 \in [-0.6, -0.3]$ and [0.3,0.6], pairing energies of neutrons are zero and thus the Fermi energies are equal to the SPE of the last occupied levels. In the spherical limit, the energy gap between the weakly bound neutron $1f_{7/2}$ and $2p_{3/2}$ orbitals is about 1 MeV, meaning that they are nearly degenerated. The strong Y_{20} correlations between these two orbitals drive this nucleus to be well deformed. This can also be interpreted that the nearly degenerated, weakly bound $1f_{7/2}$ and $2p_{3/2}$ orbitals in the spherical limit lead to the stable quadrupole deformation due to the nuclear Jahn-Teller effect [149]. The well-deformed MF ground state of ^{40}Mg results in that the low-lying excited states are rotational ones, which will be analyzed next.

The spectroscopic quadrupole moments $Q^{(s)}$ in the 2^+ and 4^+ states of ^{36,38,40}Mg obtained from DRHBc+AMP calculations with PC-F1 are shown in the top panel of Fig. 8 and compared with the results taken from Ref. [128]. From Fig. 8 it is found that calculated values of $Q^{(s)}$ with PC-F1 are well consistent with those from Ref. [128], indicating the prolate shapes of ^{36}Mg, ^{38}Mg, and ^{40}Mg. A similar conclusion can also be found in Ref. [132]. The ratios $Q^{(s)}(4^+)/Q^{(s)}(2^+)$ obtained from DRHBc+AMP calculations and Ref. [128] are presented in the bottom panel of Fig. 8 and compared with the value that corresponds to a rigid axial rotor without triaxial shapes, 1.27, labeled by the dotted blue line. One can find that all the calculated ratios are close to those of a rigid rotor. This indicates that these three nuclei are all good rotors.

In the calculated ground-state bands, the ratios $R_{4/2} = E(4^+)/E(2^+)$ are 3.50, 3.26, and 3.43, and those corresponding to the experimental values taken from Ref. [136] are 3.01, 3.10, and 2.34 for ^{36}Mg, ^{38}Mg, and ^{40}Mg, respectively. One can conclude that for ^{36}Mg and ^{38}Mg, both the experimental and calculated bands are rotational ones. For ^{40}Mg, all the above-mentioned theoretical calculations support that this nucleus is a good rotor. But this is not the case in Ref. [136], where the excitation energy of the second excited state is about 1.2 MeV, leading to the ground-state band no longer being a rotational band. Recently the MCSM calculations predicted that the ground-state band is a rotational band, and there is a state with the excitation energy of 1.2 MeV belonging to the triaxial rotational band, showing nice agreement with the experimental energy levels [139]. Future detailed studies on both the structure of SPLs and excitation spectra of ^{40}Mg by using BMF methods with considering the triaxial deformation are needed, but this is beyond the scope of the approach in the present work.

In this section we have studied the ground-state rotational bands of ^{36,38,40}Mg by using the DRHBc+AMP approach. Our calculations reproduce the low-lying excited spectra of ^{36,38,40}Mg reasonably well. For ^{40}Mg the observed first excited state is well reproduced, but the second excited state cannot be understood by the present investigation if this state belongs to the ground-state rotational band.

V. SUMMARY AND PERSPECTIVE

We have implemented the AMP based on the DRHBc theory, which can treat the large spatial extension, the contribution of continuum, deformation effects, and the coupling among them self-consistently and has been widely used to study deformed halo nuclei by solving the deformed RHB equation in the Dirac WS basis, aiming at a microscopic description of low-lying excitation of weakly bound deformed nuclei, especially for deformed halo nuclei. In the newly developed DRHBc+AMP approach, the projected wave function, the mixed densities, and currents are calculated in the Dirac WS basis. We perform careful numerical checks on convergence with respect to the parameters involved in the DRHBc+AMP method. The low-lying excited spectra of ^{36,38,40}Mg are investigated by using the DRHBc+AMP method with the density functional PC-F1. We have shown that these three nuclei, ^{36,38,40}Mg, all have pronounced prolate shape in the ground states from DRHBc calculations. The configuration of the valence neutrons for ^{38}Mg is the mixing of p- and f-wave orbitals with occupation amplitudes of 36% and 59%. ^{40}Mg is not a halo nucleus, but the configurations of the four valence neutrons have p-wave components with an occupation amplitude of 30%. The ground-state rotational bands are calculated by performing the AMP on the deformed ground-state wave function obtained from DRHBc calculations. Our results are consistent with other theoretical studies and reproduce the experimental data reasonably well. It is found that these three nuclei are all good rotors. The low-lying excited spectrum of ^{40}Mg indicates the breakdown of the shell closure at $N = 28$. It should be noted that for ^{32}Mg, similar to previous studies given in Refs. [50,112], our AMP calculations with PC-F1 in the WS basis also cannot give a reasonable description on the low-lying excitations.

It is found that the calculated excitation energy, reduced transition probability, and spectroscopic quadrupole moment with the DRHBc+AMP approach are similar to those from beyond RMF calculations with HO basis [50,132]. This is understandable because in our calculations ^{36,38,40}Mg are not halo nuclei, and the nuclear densities from the WS basis are almost the same as those from the HO basis. The point that we want to emphasize is that the proper asymptotic behavior of the wave function provided by the WS basis makes it suitable to describe halo nuclei, which is characterized by the long low-density tail and cannot be studied by expanding the wave function in terms of the HO functions. Very recently, the low-lying excitation of deformed halo nuclei were explored by our DRHBc+AMP approach and showed that the deformed halo structure persists from the ground state in the intrinsic frame to collective states [98].

In this work the density functional PC-F1 is adopted because it is convenient to compare DRHBc+AMP calculations with previous BMF calculations in Refs. [50,132]. It is also very interesting to investigate the excitation properties of weakly bound nuclei with other point-coupling density functionals, such as PC-PK1 [150], PC-X [151], and DD-PC1 [152], and such studies are in progress. In addition, it is very necessary to develop the PNP and GCM based on the DRHBc+AMP approach to restore the particle number and take into account the quantum fluctuation of collective degrees of freedom in the future.

ACKNOWLEDGMENTS

The authors would like to thank Ji-Wei Cui, Kun Wang, Zhen-Hua Zhang, Peng-Wei Zhao, and the DRHBc Mass Table Collaboration for helpful discussions and Bing-Nan Lu for sharing the MDC-RHB+AMP codes. This work has been supported by the National Key R&D Program of China (Grant No. 2018YFA0404402), the National Natural Science Foundation of China (Grants No. 11525524, No. 12070131001, No. 12047503, No. 11975237, and No. 11961141004), the Key Research Program of Frontier Sciences of Chinese Academy of Sciences (Grant No. QYZDB-SSWSYS013), and the Strategic Priority Research Program of the Chinese Academy of Sciences (Grants No. XDB34010000 and No. XDPB15). The results described in this paper are obtained on the High-Performance Computing Cluster of ITP-CAS and the ScGrid of the Supercomputing Center, Computer Network Information Center of the Chinese Academy of Sciences.

APPENDIX: MIXED DENSITIES AND CURRENTS IN COORDINATE SPACE

In coordinate space, the Dirac spinor of the Dirac WS basis is

$$\varphi_{n\kappa m}(\boldsymbol{r}sp) = i^p \frac{R_{n\kappa}(r,p)}{r}\mathcal{Y}^{l(p)}_{\kappa m}(\Omega, s), \tag{A1}$$

where $p = 1$ stands for the upper components and $p = 2$ for the lower component. $R_{n\kappa}(r,1) = G_{n\kappa}(r)$ and $R_{n\kappa}(r,2) = F_{n\kappa}(r)$ are the radial wave functions. $l(p=1) = j + \frac{1}{2}\mathrm{sgn}(\kappa)$ and $l(p=2) = j - \frac{1}{2}\mathrm{sgn}(\kappa)$.

In coordinate space, the mixed vector density for the Euler angle θ expanded in terms of the spherical harmonics is written as

$$\begin{aligned}\rho_V(\boldsymbol{r};\beta_2;\theta) &= \sum_{kk'}\rho_{k'k}(\theta)\phi^\dagger_k(\boldsymbol{r};\beta_2)\phi_{k'}(\boldsymbol{r};\beta_2)\\ &= \sum_{\lambda\mu}\rho_{V,\lambda\mu}(r;\beta_2;\theta)Y_{\lambda\mu}(\Omega),\end{aligned} \tag{A2}$$

where

$$\begin{aligned}&\rho_{V,\lambda\mu}(r;\beta_2;\theta)\\ &= \sum_{n\kappa}\sum_{n'\kappa'}\sum_{kk'}\rho_{k'k}(\theta)c^k_{n\kappa m}c^{k'}_{n'\kappa'm'}\langle\kappa m|Y^*_{\lambda\mu}(\Omega)|\kappa'm'\rangle\\ &\quad\times\frac{1}{r^2}\sum_{p=1,2}R_{n\kappa}(r,p)R_{n'\kappa'}(r,p),\end{aligned} \tag{A3}$$

and

$$\begin{aligned}&\langle\kappa m|Y_{\lambda\mu}|\kappa'm'\rangle\\ &= \sum_\sigma\int d\Omega\mathcal{Y}^{l'*}_{\kappa'm'}(\Omega,\sigma)Y_{\lambda\mu}(\Omega)\mathcal{Y}^{l}_{\kappa m}(\Omega,\sigma)\\ &= \sum_{m_l,m'_l}^{m_s,m'_s}\mathrm{C}^{j'm'}_{l'm'_l\frac{1}{2}m'_s}\mathrm{C}^{jm}_{lm_l\frac{1}{2}m_s}\sqrt{\frac{\hat\lambda\hat l}{4\pi\hat l'}}\mathrm{C}^{l'm'_l}_{\lambda\mu mm_l}\mathrm{C}^{l'0}_{\lambda 0l0},\end{aligned} \tag{A4}$$

with $\hat\lambda = 2\lambda+1$, $\hat l = 2l+1$, and $\hat l' = 2l'+1$.

Similarly, for the mixed scalar density we have

$$\rho_S(\boldsymbol{r};\beta_2;\theta) = \sum_{kk'} \rho_{k'k}(\theta)\bar{\phi}_k(\boldsymbol{r};\beta_2)\phi_{k'}(\boldsymbol{r};\beta_2)$$
$$= \sum_{\lambda\mu} \rho_{S,\lambda\mu}(r;\beta_2;\theta)Y_{\lambda\mu}(\Omega), \tag{A5}$$

where

$$\rho_{S,\lambda\mu}(r;\beta_2;\theta)$$
$$= \sum_{n\kappa}\sum_{n'\kappa'}\sum_{kk'} \rho_{k'k}(\theta)c^k_{n\kappa m}c^{k'}_{n'\kappa'm'}\langle\kappa m|Y^*_{\lambda\mu}(\Omega)|\kappa'm'\rangle$$
$$\times \sum_{p=1,2}\frac{i^{2(p-1)}}{r^2}R_{n\kappa}(r,p)R_{n'\kappa'}(r,p). \tag{A6}$$

The spatial components of the current read

$$\vec{j}(\boldsymbol{r};\beta_2;\theta) = \sum_{ij}\rho_{k'k}(\theta)\langle\phi_i|\boldsymbol{\alpha}|\phi_j\rangle$$
$$= \sum_{\lambda\mu}\vec{j}_{\lambda\mu}(r;\beta_2;\theta)Y_{\lambda\mu}(\Omega), \tag{A7}$$

with

$$\vec{j}_{\lambda\mu}(r;\beta_2;\theta)$$
$$= \sum_{ij}\sum_{n\kappa}^{n'\kappa'} c^i_{n\kappa m}c^j_{n'\kappa'm'}\rho_{k'k}(\theta)\frac{i}{r^2}\sum_{m'_l,m'_s}^{m_l,m_s}\boldsymbol{\sigma}_{m_s,m'_s}$$
$$\times\Big\{G_{n\kappa}F_{n'\kappa'}C^{jm}_{lm_l\frac{1}{2}m_s}C^{j'm'}_{\tilde{l}'m'_l\frac{1}{2}m'_s}\langle lm_l|Y^*_{\lambda\mu}(\Omega)|\tilde{l}'m'_l\rangle$$
$$-F_{n\kappa}G_{n'\kappa'}C^{jm}_{\tilde{l}m_l\frac{1}{2}m_s}C^{j'm'}_{l'm'_l\frac{1}{2}m'_s}\langle\tilde{l}m_l|Y^*_{\lambda\mu}(\Omega)|l'm'_l\rangle\Big\}. \tag{A8}$$

[1] I. Tanihata, H. Hamagaki, O. Hashimoto, Y. Shida, N. Yoshikawa, K. Sugimoto, O. Yamakawa, T. Kobayashi, and N. Takahashi, Phys. Rev. Lett. **55**, 2676 (1985).
[2] I. Tanihata, H. Savajols, and R. Kanungo, Prog. Part. Nucl. Phys. **68**, 215 (2013).
[3] A. Ozawa, T. Kobayashi, T. Suzuki, K. Yoshida, and I. Tanihata, Phys. Rev. Lett. **84**, 5493 (2000).
[4] R. V. F. Janssens, Nature (London) **459**, 1069 (2009).
[5] F. Wienholtz, D. Beck, K. Blaum, C. Borgmann, M. Breitenfeldt, R. B. Cakirli, S. George, F. Herfurth, J. D. Holt, M. Kowalska, S. Kreim, D. Lunney, V. Manea, J. Menéndez, D. Neidherr, M. Rosenbusch, L. Schweikhard, A. Schwenk, J. Simonis, J. Stanja *et al.*, Nature (London) **498**, 346 (2013).
[6] D. T. Tran, H. J. Ong, G. Hagen, T. D. Morris, N. Aoi, T. Suzuki, Y. Kanada-En'yo, L. S. Geng, S. Terashima, I. Tanihata, T. T. Nguyen, Y. Ayyad, P. Y. Chan, M. Fukuda, H. Geissel, M. N. Harakeh, T. Hashimoto, T. H. Hoang, E. Ideguchi, A. Inoue *et al.*, Nat. Commun. **9**, 1594 (2018).
[7] E. K. Warburton, J. A. Becker, and B. A. Brown, Phys. Rev. C **41**, 1147 (1990).
[8] M. Centelles, X. Roca-Maza, X. Viñas, and M. Warda, Phys. Rev. Lett. **102**, 122502 (2009).
[9] J. P. Ebran, E. Khan, T. Niksic, and D. Vretenar, Nature (London) **487**, 341 (2012).
[10] M. Freer, H. Horiuchi, Y. Kanada-En'yo, D. Lee, and Ulf-G. Meißner, Rev. Mod. Phys. **90**, 035004 (2018).
[11] M. Pfützner, M. Karny, L. V. Grigorenko, and K. Riisager, Rev. Mod. Phys. **84**, 567 (2012).
[12] A. Mutschler, A. Lemasson, O. Sorlin, D. Bazin, C. Borcea, R. Borcea, Z. Dombrádi, J.-P. Ebran, A. Gade, H. Iwasaki, E. Khan, A. Lepailleur, F. Recchia, T. Roger, F. Rotaru, D. Sohler, M. Stanoiu, S. R. Stroberg, J. A. Tostevin, M. Vandebrouck *et al.*, Nat. Phys. **13**, 152 (2016).
[13] J. Yao, H. Mei, and Z. Li, Phys. Lett. B **723**, 459 (2013).
[14] P. Cejnar, J. Jolie, and R. F. Casten, Rev. Mod. Phys. **82**, 2155 (2010).
[15] K. Heyde and J. L. Wood, Rev. Mod. Phys. **83**, 1467 (2011).
[16] Z. P. Li, T. Nikšić, and D. Vretenar, J. Phys. G: Nucl. Part. Phys. **43**, 024005 (2016).
[17] M. Bender, P.-H. Heenen, and P.-G. Reinhard, Rev. Mod. Phys. **75**, 121 (2003).
[18] S. Ćwiok, P.-H. Heenen, and W. Nazarewicz, Nature (London) **433**, 705 (2005).
[19] J. Meng, H. Toki, S. Zhou, S. Zhang, W. Long, and L. Geng, Prog. Part. Nucl. Phys. **57**, 470 (2006).
[20] J. Meng and S.-G. Zhou, J. Phys. G: Nucl. Part. Phys. **42**, 093101 (2015).
[21] T. Nikšić, D. Vretenar, and P. Ring, Prog. Part. Nucl. Phys. **66**, 519 (2011).
[22] *Relativistic Density Functional for Nuclear Structure*, edited by J. Meng (World Scientific, Singapore, 2016).
[23] S.-G. Zhou, Phys. Scr. **91**, 063008 (2016).
[24] S.-G. Zhou, PoS **INPC2016**, 373 (2017).
[25] T. Otsuka, A. Gade, O. Sorlin, T. Suzuki, and Y. Utsuno, Rev. Mod. Phys. **92**, 015002 (2020).
[26] E. Caurier, G. Martínez-Pinedo, F. Nowack, A. Poves, and A. P. Zuker, Rev. Mod. Phys. **77**, 427 (2005).
[27] D. Vretenar, A. V. Afanasjev, G. A. Lalazissis, and P. Ring, Phys. Rep. **409**, 101 (2005).
[28] M. Kimura, T. Suhara, and Y. Kanada-En'yo, Eur. Phys. J. A **52**, 373 (2016).
[29] C. H. Greene, P. Giannakeas, and J. Pérez-Ríos, Rev. Mod. Phys. **89**, 035006 (2017).
[30] J. L. Egido, Phys. Scr. **91**, 073003 (2016).
[31] W. Nazarewicz, Nat. Phys. **14**, 537 (2018).
[32] P. Ring and P. Schuck, *The Nuclear Many-Body Problem* (Springer-Verlag, Berlin, Heidelberg, 1980).
[33] *Energy Density Functional Methods for Atomic Nuclei*, edited by N. Schunck, IOP Expanding Physics Series (IOP Publishing, Bristol, England, 2019).
[34] L. M. Robledo, T. R. Rodríguez, and R. R. Rodríguez-Guzmán, J. Phys. G: Nucl. Part. Phys. **46**, 013001 (2019).
[35] J. A. Sheikh, J. Dobaczewski, P. Ring, L. M. Robledo, and C. Yannouleas, J. Phys. G: Nucl. Part. Phys. **48**, 123001 (2021).

[36] R. R. Rodríguez-Guzmán, J. L. Egido, and L. M. Robledo, Phys. Rev. C **62**, 054308 (2000).
[37] M. Bender, H. Flocard, and P. H. Heenen, Phys. Rev. C **68**, 044321 (2003).
[38] M. Bender, P. Bonche, T. Duguet, and P.-H. Heenen, Phys. Rev. C **69**, 064303 (2004).
[39] R. R. Rodríguez-Guzmán, J. L. Egido, and L. M. Robledo, Phys. Rev. C **69**, 054319 (2004).
[40] M. Bender, P. Bonche, and P.-H. Heenen, Phys. Rev. C **74**, 024312 (2006).
[41] T. R. Rodríguez and J. L. Egido, Phys. Rev. Lett. **99**, 062501 (2007).
[42] T. Nikšić, D. Vretenar, G. A. Lalazissis, and P. Ring, Phys. Rev. Lett. **99**, 092502 (2007).
[43] T. R. Rodríguez and J. L. Egido, Phys. Lett. B **663**, 49 (2008).
[44] J.-W. Cui, X.-R. Zhou, and H.-J. Schulze, Phys. Rev. C **91**, 054306 (2015).
[45] J.-W. Cui, X.-R. Zhou, L.-X. Guo, and H.-J. Schulze, Phys. Rev. C **95**, 024323 (2017).
[46] H. Mei, K. Hagino, J. M. Yao, and T. Motoba, Phys. Rev. C **97**, 064318 (2018).
[47] H.-J. Xia, X.-Y. Wu, H. Mei, and J.-M. Yao, Sci. China Phys. Mech. Astron. **62**, 42011 (2019).
[48] M. Bender and P.-H. Heenen, Phys. Rev. C **78**, 024309 (2008).
[49] T. R. Rodríguez and J. L. Egido, Phys. Rev. C **81**, 064323 (2010).
[50] J. M. Yao, J. Meng, P. Ring, and D. Pena Arteaga, Phys. Rev. C **79**, 044312 (2009).
[51] J. M. Yao, J. Meng, P. Ring, and D. Vretenar, Phys. Rev. C **81**, 044311 (2010).
[52] J. M. Yao, K. Hagino, Z. P. Li, J. Meng, and P. Ring, Phys. Rev. C **89**, 054306 (2014).
[53] J. L. Egido, M. Borrajo, and T. R. Rodríguez, Phys. Rev. Lett. **116**, 052502 (2016).
[54] F.-Q. Chen and J. L. Egido, Phys. Rev. C **95**, 024307 (2017).
[55] J. M. Yao, E. F. Zhou, and Z. P. Li, Phys. Rev. C **92**, 041304(R) (2015).
[56] R. Rodríguez-Guzmán, L. M. Robledo, and P. Sarriguren, Phys. Rev. C **86**, 034336 (2012).
[57] R. Rodríguez-Guzmán, Y. M. Humadi, and L. M. Robledo, J. Phys. G: Nucl. Part. Phys. **48**, 015103 (2020).
[58] R. Rodríguez-Guzmán and L. M. Robledo, Phys. Rev. C **103**, 044301 (2021).
[59] P. Marević and N. Schunck, Phys. Rev. Lett. **125**, 102504 (2020).
[60] J. L. Egido and A. Jungclaus, Phys. Rev. Lett. **125**, 192504 (2020).
[61] J. L. Egido and A. Jungclaus, Phys. Rev. Lett. **126**, 192501 (2021).
[62] B. Bally, B. Avez, M. Bender, and P.-H. Heenen, Phys. Rev. Lett. **113**, 162501 (2014).
[63] M. Borrajo and J. L. Egido, Euro. Phys. J. A **52**, 277 (2016).
[64] M. Borrajo and J. L. Egido, Phys. Lett. B **764**, 328 (2017).
[65] M. Borrajo and J. L. Egido, Phys. Rev. C **98**, 044317 (2018).
[66] W. Pannert, P. Ring, and J. Boguta, Phys. Rev. Lett. **59**, 2420 (1987).
[67] C. E. Price and G. E. Walker, Phys. Rev. C **36**, 354 (1987).
[68] Y. Gambhir, P. Ring, and A. Thimet, Ann. Phys. **198**, 132 (1990).
[69] M. Stoitsov, P. Ring, D. Vretenar, and G. A. Lalazissis, Phys. Rev. C **58**, 2086 (1998).
[70] S.-G. Zhou, J. Meng, S. Yamaji, and S.-C. Yang, Chin. Phys. Lett. **17**, 717 (2000).
[71] S.-G. Zhou, J. Meng, and P. Ring, Phys. Rev. C **68**, 034323 (2003).
[72] Y. N. Zhang, J. C. Pei, and F. R. Xu, Phys. Rev. C **88**, 054305 (2013).
[73] P. G. Hansen and B. Jonson, Europhys. Lett. **4**, 409 (1987).
[74] J. Dobaczewski, W. Nazarewicz, T. R. Werner, J. F. Berger, C. R. Chinn, and J. Dechargé, Phys. Rev. C **53**, 2809 (1996).
[75] J. Meng and P. Ring, Phys. Rev. Lett. **77**, 3963 (1996).
[76] J. Meng and P. Ring, Phys. Rev. Lett. **80**, 460 (1998).
[77] J. Meng, Nucl. Phys. A **635**, 3 (1998).
[78] A. S. Jensen, K. Riisager, D. V. Fedorov, and E. Garrido, Rev. Mod. Phys. **76**, 215 (2004).
[79] K. Riisager, Phys. Scr. **2013**, 014001 (2013).
[80] J. Dobaczewski, H. Flocard, and J. Treiner, Nucl. Phys. A **422**, 103 (1984).
[81] W. Pöschl, D. Vretenar, and P. Ring, Comput. Phys. Commun. **103**, 217 (1997).
[82] S. Typel, Front. Phys. **6**, 73 (2018).
[83] H. Nakada and K. Takayama, Phys. Rev. C **98**, 011301(R) (2018).
[84] M. V. Stoitsov, W. Nazarewicz, and S. Pittel, Phys. Rev. C **58**, 2092 (1998).
[85] W. Pöschl, D. Vretenar, G. A. Lalazissis, and P. Ring, Phys. Rev. Lett. **79**, 3841 (1997).
[86] J. Meng, I. Tanihata, and S. Yamaji, Phys. Lett. B **419**, 1 (1998).
[87] W. H. Long, P. Ring, J. Meng, N. Van Giai, and C. A. Bertulani, Phys. Rev. C **81**, 031302(R) (2010).
[88] T. Nakamura, N. Kobayashi, Y. Kondo, Y. Satou, N. Aoi, H. Baba, S. Deguchi, N. Fukuda, J. Gibelin, N. Inabe, M. Ishihara, D. Kameda, Y. Kawada, T. Kubo, K. Kusaka, A. Mengoni, T. Motobayashi, T. Ohnishi, M. Ohtake, N. A. Orr *et al.*, Phys. Rev. Lett. **103**, 262501 (2009).
[89] T. Nakamura, N. Kobayashi, Y. Kondo, Y. Satou, J. A. Tostevin, Y. Utsuno, N. Aoi, H. Baba, N. Fukuda, J. Gibelin, N. Inabe, M. Ishihara, D. Kameda, T. Kubo, T. Motobayashi, T. Ohnishi, N. A. Orr, H. Otsu, T. Otsuka, H. Sakurai *et al.*, Phys. Rev. Lett. **112**, 142501 (2014).
[90] N. Kobayashi, T. Nakamura, Y. Kondo, J. A. Tostevin, Y. Utsuno, N. Aoi, H. Baba, R. Barthelemy, M. A. Famiano, N. Fukuda, N. Inabe, M. Ishihara, R. Kanungo, S. Kim, T. Kubo, G. S. Lee, H. S. Lee, M. Matsushita, T. Motobayashi, T. Ohnishi *et al.*, Phys. Rev. Lett. **112**, 242501 (2014).
[91] S.-G. Zhou, J. Meng, P. Ring, and E.-G. Zhao, Phys. Rev. C **82**, 011301(R) (2010).
[92] J. C. Pei, Y. N. Zhang, and F. R. Xu, Phys. Rev. C **87**, 051302(R) (2013).
[93] Y. Chen, P. Ring, and J. Meng, Phys. Rev. C **89**, 014312 (2014).
[94] L.-L. Li, J. Meng, P. Ring, E.-G. Zhao, and S.-G. Zhou, Phys. Rev. C **85**, 024312 (2012).
[95] X.-X. Sun, J. Zhao, and S.-G. Zhou, Phys. Lett. B **785**, 530 (2018).
[96] K. Y. Zhang, D. Y. Wang, and S. Q. Zhang, Phys. Rev. C **100**, 034312 (2019).
[97] X.-X. Sun, J. Zhao, and S.-G. Zhou, Nucl. Phys. A **1003**, 122011 (2020).
[98] X.-X. Sun and S.-G. Zhou, Sci. Bull. **66**, 2072 (2021).
[99] P. G. Reinhard, Rep. Prog. Phys. **52**, 439 (1989).

[100] P. Ring, Prog. Part. Nucl. Phys. **37**, 193 (1996).
[101] H. Liang, J. Meng, and S.-G. Zhou, Phys. Rep. **570**, 1 (2015).
[102] J. Meng, H. Toki, J. Y. Zeng, S. Q. Zhang, and S.-G. Zhou, Phys. Rev. C **65**, 041302(R) (2002).
[103] X. L. Lu, B. Y. Sun, and W. H. Long, Phys. Rev. C **87**, 034311 (2013).
[104] Z. H. Yang, Y. Kubota, A. Corsi, K. Yoshida, X.-X. Sun, J. G. Li, M. Kimura, N. Michel, K. Ogata, C. X. Yuan, Q. Yuan, G. Authelet, H. Baba, C. Caesar, D. Calvet, A. Delbart, M. Dozono, J. Feng, F. Flavigny, J.-M. Gheller *et al.*, Phys. Rev. Lett. **126**, 082501 (2021).
[105] X.-X. Sun, Phys. Rev. C **103**, 054315 (2021).
[106] K. Zhang, M.-K. Cheoun, Y.-B. Choi, P. S. Chong, J. Dong, L. Geng, E. Ha, X. He, C. Heo, M. C. Ho, E. J. In, S. Kim, Y. Kim, C.-H. Lee, J. Lee, Z. Li, T. Luo, J. Meng, M.-H. Mun, Z. Niu, Phys. Rev. C **102**, 024314 (2020).
[107] E. J. In, P. Papakonstantinou, Y. Kim, and S.-W. Hong, Int. J. Mod. Phys. E **30**, 2150009 (2021).
[108] K. Zhang, X. He, J. Meng, C. Pan, C. Shen, C. Wang, and S. Zhang, Phys. Rev. C **104**, L021301 (2021).
[109] C. Pan, K. Y. Zhang, P. S. Chong, C. Heo, M. C. Ho, J. Lee, Z. P. Li, W. Sun, C. K. Tam, S. H. Wong, R. W.-Y. Yeung, T. C. Yiu, and S. Q. Zhang, Phys. Rev. C **104**, 024331 (2021).
[110] X.-T. He, C. Wang, K.-Y. Zhang, and C.-W. Shen, Chin. Phys. C **45**, 101001 (2021).
[111] T. Nikšić, D. Vretenar, and P. Ring, Phys. Rev. C **73**, 034308 (2006).
[112] T. Nikšić, D. Vretenar, and P. Ring, Phys. Rev. C **74**, 064309 (2006).
[113] H. Xia, H. Mei, and J. Yao, Sci. China Phys. Mech. Astron. **60**, 102021 (2017).
[114] B.-N. Lu, E.-G. Zhao, and S.-G. Zhou, Phys. Rev. C **85**, 011301(R) (2012).
[115] B.-N. Lu, J. Zhao, E.-G. Zhao, and S.-G. Zhou, Phys. Rev. C **89**, 014323 (2014).
[116] J. Zhao, B.-N. Lu, E.-G. Zhao, and S.-G. Zhou, Phys. Rev. C **95**, 014320 (2017).
[117] K. Wang and B.-N. Lu, Commun. Theor. Phys. (to be published), doi:10.1088/1572-9494/ac3999.
[118] L.-L. Li, J. Meng, P. Ring, E.-G. Zhao, and S.-G. Zhou, Chin. Phys. Lett. **29**, 042101 (2012).
[119] Y. Chen, L. Li, H. Liang, and J. Meng, Phys. Rev. C **85**, 067301 (2012).
[120] H. Kucharek and P. Ring, Z. Phys. A **339**, 23 (1991).
[121] W. Koepf and P. Ring, Z. Phys. A **339**, 81 (1991).
[122] J. P. Blaizot and G. Ripka, *Quantum Theory of Finite Systems* (The MIT Press, Cambridge, MA, 1985).
[123] K. Hara and Y. Sun, Int. J. Mod. Phys. E **4**, 637 (1995).
[124] A. Valor, P.-H. Heenen, and P. Bonche, Nucl. Phys. A **671**, 145 (2000).
[125] R. Balian and E. Brezin, Il Nuovo Cimento B (1965-1970) **64**, 37 (1969).
[126] N. Onishi and S. Yoshida, Nucl. Phys. **80**, 367 (1966).
[127] P. Bonche, J. Dobaczewski, H. Flocard, P.-H. Heenen, and J. Meyer, Nucl. Phys. A **510**, 466 (1990).
[128] R. Rodríguez-Guzmán, J. L. Egido, and L. M. Robledo, Nucl. Phys. A **709**, 201 (2002).
[129] J. M. Yao, M. Bender, and P.-H. Heenen, Phys. Rev. C **91**, 024301 (2015).
[130] T. Bürvenich, D. G. Madland, J. A. Maruhn, and P.-G. Reinhard, Phys. Rev. C **65**, 044308 (2002).
[131] C. Pan, K. Zhang, and S. Zhang, Int. J. Mod. Phys. E **28**, 1950082 (2019).
[132] J. M. Yao, H. Mei, H. Chen, J. Meng, P. Ring, and D. Vretenar, Phys. Rev. C **83**, 014308 (2011).
[133] R. R. Rodríguez-Guzmán, J. Egido, and L. Robledo, Phys. Lett. B **474**, 15 (2000).
[134] K. Hagino, P.-G. Reinhard, and G. F. Bertsch, Phys. Rev. C **65**, 064320 (2002).
[135] P. Doornenbal, H. Scheit, S. Takeuchi, N. Aoi, K. Li, M. Matsushita, D. Steppenbeck, H. Wang, H. Baba, H. Crawford, C. R. Hoffman, R. Hughes, E. Ideguchi, N. Kobayashi, Y. Kondo, J. Lee, S. Michimasa, T. Motobayashi, H. Sakurai, M. Takechi *et al.*, Phys. Rev. Lett. **111**, 212502 (2013).
[136] H. L. Crawford, P. Fallon, A. O. Macchiavelli, P. Doornenbal, N. Aoi, F. Browne, C. M. Campbell, S. Chen, R. M. Clark, M. L. Cortés, M. Cromaz, E. Ideguchi, M. D. Jones, R. Kanungo, M. MacCormick, S. Momiyama, I. Murray, M. Niikura, S. Paschalis, M. Petri *et al.*, Phys. Rev. Lett. **122**, 052501 (2019).
[137] H. Nakada, Phys. Rev. C **87**, 014336 (2013).
[138] G. X. Dong, X. B. Wang, H. L. Liu, and F. R. Xu, Phys. Rev. C **88**, 024328 (2013).
[139] N. Tsunoda, T. Otsuka, K. Takayanagi, N. Shimizu, T. Suzuki, Y. Utsuno, S. Yoshida, and H. Ueno, Nature (London) **587**, 66 (2020).
[140] T. R. Rodríguez, Eur. Phys. J. A **52**, 190 (2016).
[141] M. Shimada, S. Watanabe, S. Tagami, T. Matsumoto, Y. R. Shimizu, and M. Yahiro, Phys. Rev. C **93**, 064314 (2016).
[142] X.-Y. Wu and X.-R. Zhou, Phys. Rev. C **92**, 054321 (2015).
[143] S. Watanabe, K. Minomo, M. Shimada, S. Tagami, M. Kimura, M. Takechi, M. Fukuda, D. Nishimura, T. Suzuki, T. Matsumoto, Y. R. Shimizu, and M. Yahiro, Phys. Rev. C **89**, 044610 (2014).
[144] M. Takechi, S. Suzuki, D. Nishimura, M. Fukuda, T. Ohtsubo, M. Nagashima, T. Suzuki, T. Yamaguchi, A. Ozawa, T. Moriguchi, H. Ohishi, T. Sumikama, H. Geissel, M. Ishihara, N. Aoi, R.-J. Chen, D.-Q. Fang, N. Fukuda, S. Fukuoka, H. Furuki *et al.*, EPJ Web Conf. **66**, 02101 (2014).
[145] M. Wang, G. Audi, F. Kondev, W. Huang, S. Naimi, and X. Xu, Chin. Phys. C **41**, 30003 (2017).
[146] M. Wang, W. Huang, F. Kondev, G. Audi, and S. Naimi, Chin. Phys. C **45**, 030003 (2021).
[147] H. Kasuya and K. Yoshida, Prog. Theo. Exp. Phys. **2021**, 013D01 (2021).
[148] T.-T. Sun, L. Qian, C. Chen, P. Ring, and Z. P. Li, Phys. Rev. C **101**, 014321 (2020).
[149] P.-G. Reinhard and E. Otten, Nucl. Phys. A **420**, 173 (1984).
[150] P. W. Zhao, Z. P. Li, J. M. Yao, and J. Meng, Phys. Rev. C **82**, 054319 (2010).
[151] A. Taninah, S. E. Agbemava, A. V. Afanasjev, and P. Ring, Phys. Lett. B **800**, 135065 (2020).
[152] T. Nikšić, D. Vretenar, and P. Ring, Phys. Rev. C **78**, 034318 (2008).